

# Robust Image-Based Landing Control of a Quadrotor on an Unpredictable Moving Vehicle Using Circle Features

Jie Lin<sup>1</sup>, Yaonan Wang<sup>1</sup>, Zhiqiang Miao<sup>1</sup>, *Member, IEEE*, Hesheng Wang<sup>2</sup>, *Senior Member, IEEE*,  
and Rafael Fierro<sup>3</sup>, *Senior Member, IEEE*

**Abstract**—This paper addresses the landing problem of a quadrotor on an unpredictable moving vehicle, using a robust image-based visual servoing (IBVS) method. The circle-based image moments are defined to construct image dynamics, and the passivity-like property of the circle features is preserved by reprojecting to the virtual image plane. The landing control system is decoupled into translation and rotation modules due to the rotation invariance of the proposed circle features. First, by exploiting the error transformation in the image space, a robust IBVS controller can overcome the lack of both the desired depth information of target features and the velocity feedback of the target. Next, an adaptive geometric attitude controller is developed directly using rotation matrices to avoid the singularities of Euler-angles and the ambiguity of quaternions. One benefit of the proposed scheme is that it can potentially improve the camera visibility, guarantee the transient and steady-state behaviors in image space, and be efficiently implemented on the low-cost quadrotor. Finally, The stability analysis is presented using Lyapunov stability theory on cascaded systems, and the effectiveness of the proposed control strategy is demonstrated through simulations and experiments.

**Note to Practitioners**—The motivation of this paper is to investigate a practical control strategy for the image-based

landing control of underactuated quadrotors on an unpredictable moving vehicle. In most of the existing image-based landing control schemes for underactuated quadrotors, having the prior predictive model of the moving landing vehicle to provide a feed-forward compensation during the landing maneuver. However, due to the fact that the landing environment and vehicle are primarily stochastic, resulting in no predictive models are valid in practice. Therefore, this paper suggests a robust image-based landing control strategy without the model or state of the moving landing vehicle. In particular, a novel virtual circle feature, possessing the characteristic of rotation invariance, is designed for the landing of underactuated quadrotors, which decouples the landing system and simplifies the control design. Moreover, the image feature errors are directly retained within prescribed performance funnels in the image space. As a result, the transient and steady-state landing behaviors can be implicitly guaranteed in Cartesian space. The stability and convergence of the system are analyzed mathematically and the experiment using quadrotors provides promising results. In ongoing research, we are addressing the issues of collision avoidances and unknown disturbances to provide a more realistic setup for the autonomous deployment and recovery of underactuated quadrotors in GPS-denied environments.

**Index Terms**—Automatic landing, image-based visual servoing, nonlinear control, quadrotor, unmanned aerial vehicle (UAV).

Manuscript received March 21, 2022; revised April 28, 2022; accepted June 1, 2022. This article was recommended for publication by Associate Editor G. Palli and Editor J. Yi upon evaluation of the reviewers' comments. This work was supported in part by the National Key Research and Development Program of China under Grant 2021YFB1714700, in part by the Natural Science Foundation of China under Grant 61733004 and Grant 61903135, in part by the Postgraduate Scientific Research Innovation Project of Hunan Province under Grant QL20210080, in part by the Natural Science Foundation of Hunan Province under Grant 2021JJ20029, in part by the Science and Technology Innovation Program of Hunan Province under Grant 2021RC3060, and in part by the Youth Talent Support Project of the Chinese Association for Science and Technology. (*Corresponding author: Zhiqiang Miao.*)

Jie Lin, Yaonan Wang, and Zhiqiang Miao are with the College of Electrical and Information Engineering, Hunan University, Changsha 410082, China, and also with the National Engineering Laboratory for Robot Visual Perception and Control, Changsha 410082, China (e-mail: linjie0275@hnu.edu.cn; yaonan@hnu.edu.cn; miaozhiqiang@hnu.edu.cn).

Hesheng Wang is with the Department of Automation and the Key Laboratory of System Control and Information Processing, Ministry of Education of China, Shanghai Jiao Tong University, Shanghai 200240, China, and also with the State Key Laboratory of Robotics and System, Harbin Institute of Technology, Harbin 150001, China (e-mail: wanghesheng@sjtu.edu.cn).

Rafael Fierro is with the MARHES Laboratory, Department of Electrical and Computer Engineering, The University of New Mexico, Albuquerque, NM 87131 USA (e-mail: rfierro@unm.edu).

This article has supplementary material provided by the authors and color versions of one or more figures available at <https://doi.org/10.1109/TASE.2022.3180506>.

Digital Object Identifier 10.1109/TASE.2022.3180506

## I. INTRODUCTION

THE autonomous control of unmanned aerial vehicles (UAVs) is an active and challenging field of research, which has attracted significant attention recently in numerous civilian and military applications, such as industrial inspection, site surveillance, or search and rescue operations [1]–[3]. UAV autonomous control has been proven to be advantageous for dangerous and high-precision missions over human operators. In particular, quadrotors serve as the ideal aerial platforms suited for the development of autonomous systems because of the high-mobility capabilities to hover and take off and land vertically, as depicted in [4], [5]. With the increasing interest in quadrotors to offer effective and large-scale services, it is important to realize the automation of quadrotors with less cost, weight, and human involvement.

Due to the increasingly accurate and reliable technology in sensing, different onboard sensors have been vastly developed to address the localization of quadrotors. A traditional pose measured from the inertial measurement unit (IMU) or global position system (GPS) is sufficient for general applications,

but the local accuracy is unsuitable for a precision landing [6]. In addition, they are increasing in offering a wide scope of applications intended to extend well beyond GPS environments. Some works employing laser range finders or LIDAR increased the energetic cost of staying airborne to obtain enough space information [7], [8]. However, one sensor that is becoming increasingly popular for UAVs is lightweight onboard monocular cameras, which can provide richer information at a lower cost [9]. Considerable effort has been devoted to vision-based control of UAVs, and visual servo approaches are generally classified into two main classes: position-based visual servoing (PBVS) [10]–[18] and image-based visual servoing (IBVS) [19]–[22]. The PBVS focuses on the explicit calculation of 3-D pose estimation from the known target markers [10], and a large variety of fiducial markers have been proposed including point marker [11], roundel marker [12], aruco marker [13], and apriltag [14]. The case of combining a Kalman filter by using additional sensors was presented in [15]–[18]. Although the pose measurements of the PBVS is intuitive in 3-D space, it raises the computation burden of low-cost quadrotors. Different from PBVS, the IBVS makes use of image features directly such that tasks are implicitly accomplished in Cartesian space when the image features converge to the desired configuration in the image space [19]. Although it needs feature depths to link the spatial velocity of the camera to the temporal variation of the selected image features [20]–[22], it is insensitive to the feature depth and the camera calibration errors.

It is well known that proper feature extraction is essential to the performance of IBVS. Especially, quadrotors, as a kind of thrust vectored vehicles, have six degrees of freedom and only four inputs. Its strongly coupled dynamics raises some technical issues in the IBVS design [23], [24], based on IBVS theory, several appropriate image features have been widely investigated to overcome the underactuated nature of quadrotors, mainly including spherical image moments [25]–[30] and virtual image moments [31]–[42]. In [25], the spherical image moments were shown to be effective in decoupling the position and orientation dynamics of the quadrotor system, using the passivity-like properties of spherical camera geometry. In [26], it was demonstrated that the conventionally spherical image moments exist in an ill-conditioned feedback matrix. Thus, this work has been modified in [27]–[29] by rescaling the image features to redefine the error criterion. The case has been tested in a real experiment by [30]. However, It is worth noting the limitations of spherical image moments, which perform undesired behavior in the vertical axis because of the nature of the spherical camera geometry. Moreover, the moment invariants have been well studied for visual servoing in [31], which has good decoupling and linearizing properties when the object is parallel to the image plane. In [32]–[35], a virtual image moment was developed for the visual servoing of the quadrotors, and it transformed the real image plane to a virtual image plane through a rotation matrix to make the quadrotor be always parallel to the planar target lying on the level ground. Thus, the virtual image moment has the constant advantage of decoupling. A modified work was to plan the trajectory on the virtual image plane in [36]. In [37]–[39],

the visual target was kept in the real camera's field of view using the virtual camera approach. These works were further extended to track a moving target in [40]–[42].

In most of the aforementioned studies, the proposed landing control schemes have been traditionally focused on predictable landing vehicles, and it assumes that relative states are available for feedback. The position and velocity of the ground target were transmitted to the quadrotor through a communication sensor in [16]. Some works exploited a reliable predictive model of the motion of the landing vehicle to provide a feed-forward compensation during the landing maneuver. In [6], [42], the vertical motions of the landing target were modeled as a superposition of several sine functions. In [17], [18], a car-like model was adopted to predict the future motion of vehicles. However, due to the random landing vehicles and limited computational resources, it suffers from the disadvantage that predictable vehicle models are difficult to obtain in reality. In [35], an adaptive rule was described to account for the lack of linear velocity of the ground target. However, it is only considered kinematic control. In [28], the optic flow was used for aerial robots to provide relative velocity. The case with bounded linear accelerations of the target was considered in [29] to widen the range of applicability, but it is not always available in reality due to the hypothesis of invariable gray level and inaccurate velocity measurements. In [41], the filter-like auxiliary dynamic system was designed to solve the relative velocity. In [40], a tracking-differentiator observer was developed to estimate the target's parameters.

In this paper, a robust image-based control approach is proposed to address the autonomous landing of underactuated quadrotors on an unpredictable moving vehicle. The landing control of the quadrotor involves a hierarchical control paradigm with the outer-loop IBVS controller governing the translation, and the inner-loop controller regulating the attitude. Motivated by the funnel control approaches that have excellent prescribed performance in Cartesian space [43], we creatively introduced funnel functions to design error transformation in the image space to enhance the robustness against uncertain systems. Using Lyapunov tools on cascaded systems, the stability of the closed-loop control system is guaranteed. Preliminary results in this paper have been presented in [44]. In this paper, detailed theoretical analysis and extensive simulation and experimental results have been presented to support the developed control strategy. Compared with other image-based quadrotors landing works, the main contributions of this article can be summarized as follows:

- i) By exploiting the circle feature in the virtual image plane, the image dynamics possesses the characteristic of rotation invariance to conquer the underactuated nature of quadrotors. Different from the classic virtual camera method used point features in [33]–[42], it is independent of yaw angle and thus simplifies control design. What's more, it is more robust for the motion blur and the partial occlusion. The spherical image moments applied in [22], [27]–[29] are also rotation invariance, but each point projected onto the spherical image plane has a different depth value, thus resulting in undesired behavior in the vertical axis. In contrast, our method can

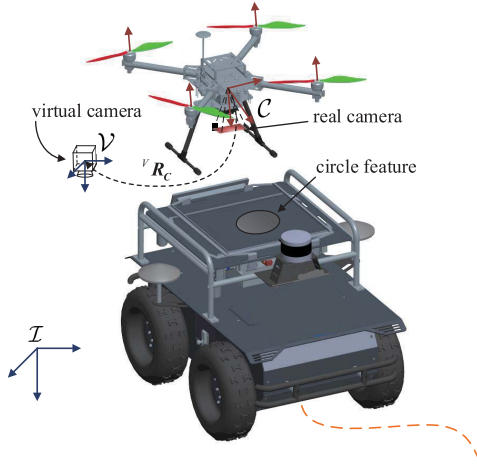


Fig. 1. System overview and frames of reference used.

improve the tracking trajectory quality of the quadrotor effectively.

- ii) The designed robust IBVS controller can overcome the lack of both desired depth information of features and velocity measurements of targets. Furthermore, a relaxed assumption for practical applications only requires the velocity of the unpredictable targets is bounded. While in [6], [17], [18], [42], the target model was known and its velocity was required to be sufficiently smooth. In [40], [41], the desired depth values were assumed to be known and additional observers were used to estimate the velocity information of the target. On the other hand, by designing the favorable error transformation for the image feature, the proposed controller can potentially improve the camera visibility and guarantee the transient and steady-state behaviors in Cartesian space.
- iii) A geometric attitude controller is developed directly using rotation matrices to avoid the singularities of Euler-angles and the ambiguity of quaternions. In particular, due to the unknown target velocity, the derivative of the quadrotor thrust is unavailable (hence the desired angular velocity can't be defined). To this end, a command filter is designed to obtain the derivative of the thrust so that the desired angular velocity implemented in the attitude controller can be well-defined.

The remainder of this paper is organized as follows. Section II introduces system modeling and problem statements. Section III presents the control design and stability analysis. Simulation and experimental results to verify the effectiveness of the proposed control method are shown in Section IV. Section V concludes the paper.

## II. PROBLEM FORMULATION

### A. System Description and Modelling

In our consideration, an autonomic landing system is designed for many applications of interest, which is composed of a quadrotor UAV equipped with a monocular camera and an IMU, and a ground vehicle posted with a circular visual feature, as shown in Fig. 1. The motion of the quadrotor

is described in two coordinated frames: the inertia frame  $\mathcal{I}$  and the body-fixed frame  $\mathcal{B}$  whose origin is located in the mass center of the quadrotor. Denote  $\mathbf{p} \in \mathbb{R}^3$  and  $\mathbf{v} \in \mathbb{R}^3$  are the position and velocity vector of quadrotor expressed in  $\mathcal{I}$ ,  $\mathbf{R} \in \mathbb{R}^{3 \times 3}$  is the rotation matrix from its body-fixed frame to the inertial frame, and  $\boldsymbol{\Omega} \in \mathbb{R}^3$  is the angular velocity expressed in  $\mathcal{B}$ . Based on Euler-Newton formulae, the dynamics of the quadrotor is described as

$$\dot{\mathbf{p}} = \mathbf{v}, \quad (1)$$

$$m\dot{\mathbf{v}} = -f\mathbf{R}\mathbf{i}_3 + m\mathbf{g}\mathbf{i}_3, \quad (2)$$

$$\dot{\mathbf{R}} = \mathbf{R}\boldsymbol{\Omega}^\wedge, \quad (3)$$

$$\mathbf{J}\dot{\boldsymbol{\Omega}} = -\boldsymbol{\Omega}^\wedge \mathbf{J}\boldsymbol{\Omega} + \boldsymbol{\tau}, \quad (4)$$

where the physical properties of the quadrotor are defined by the total mass  $m$ , gravity acceleration  $g$ , and constant symmetric inertia matrix  $\mathbf{J} = \text{diag}(J_x, J_y, J_z) \in \mathbb{R}^{3 \times 3}$ ;  $f$  and  $\boldsymbol{\tau} \in \mathbb{R}^3$  represent the net thrust force and the torque inputs, respectively. The constant vector  $\mathbf{i}_3 = [0, 0, 1]^T$  is the thrust orientation, and  $g$  is the gravitational acceleration. The operator  $(\cdot)^\wedge : \mathbb{R}^3 \mapsto \mathfrak{so}(3)$  is defined such that  $(x)^\wedge y = x \times y$  for all  $x, y \in \mathbb{R}^3$ , where  $\times$  denotes the cross product. The inverse of  $(\cdot)^\wedge : \mathfrak{so}(3) \mapsto \mathbb{R}^3$  is denoted by  $(\cdot)^\vee$ .

A circular visual feature lies on a textured plane of the ground vehicle called the target plane, which is assumed to be horizontal and visible at the initial moment. A look-down camera is rigidly attached to the center of mass of the vehicle so that  $\mathcal{C}$  coincides with  $\mathcal{B}$ . Instead of measuring and estimating the velocity of the moving vehicle, we only assume that:

*Assumption 1:* The linear velocity of the ground vehicle  $\mathbf{v}_t \in \mathbb{R}^3$  is unknown, but there is an unknown real positive constant  $\bar{v}_t$  such that  $\|\mathbf{v}_t\| < \bar{v}_t$ .

### B. Visual Features and Dynamics

In this section, image features and their dynamics implemented in the IBVS scheme are presented. To obtain a decoupled link between the image space and the task space, we introduce the perspective projection image moments. The various image moments can be summarized into two types: point-based and region-based image moments. Though three noncollinear points are enough to define the image moments, the point feature is unreliable because of the motion blur and the partial occlusion, especially for the visual servoing task of the quadrotor in the 3-D space. We observe that the circle feature, as a special type of region-based image feature, has the geometric characteristics of center symmetry so that it has the advantage of yaw angle invariance compared with the point feature when the quadrotor is parallel to the target plane.

A natural idea is to apply a virtual rotation to the real camera so that the image plane in its virtual desired position is parallel to the target plane, such a configuration is usually called a virtual image plane, as shown in Fig. 2. The angle invariance of the circle feature will be enlarged in this configuration. The circle feature of the target plane can be defined by a set of closed contours in the virtual image plane, next, we give the image dynamics based on a circle feature. Firstly, the mapping



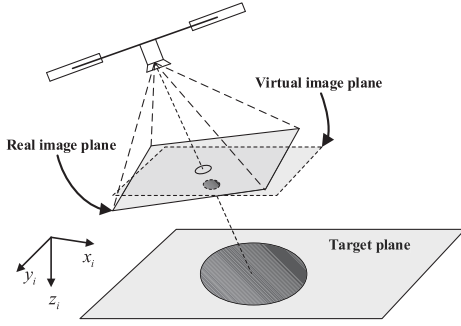


Fig. 2. Geometry relationship between the real image plane, the virtual image plane, and the target plane.

from an observed point  $\mathbf{P}_C = [X_C, Y_C, Z_C]^T$  in  $\mathcal{C}$  to an image coordinate  $\mathbf{q}_c = [m_c, n_c]^T$  using a perspective camera model is given by

$$\mathbf{q}_c = \begin{bmatrix} m_c \\ n_c \end{bmatrix} = \frac{f_c}{Z_C} \begin{bmatrix} X_C \\ Y_C \end{bmatrix}. \quad (5)$$

where  $f_c > 0$  is the focal length of the camera.

A virtual camera frame  $\mathcal{V}$  is designed to inherit the translation but not the rotation of  $\mathcal{C}$ , its origin coincides with the real camera frame. Similarly, a point is described as  $\mathbf{P}_V = [X_V, Y_V, Z_V]^T$  in  $\mathcal{V}$ , and the corresponding image coordinate is  $\mathbf{q}_v = [m_v, n_v]^T$ . It's clear that the rotation matrix  ${}^I\mathbf{R}_V$  from  $\mathcal{V}$  to  $\mathcal{I}$  is the identity matrix as  $\mathbf{I}_3 \in SO(3)$ , then  $\mathbf{P}_V = \mathbf{R}\mathbf{P}_C$ . Denoted  $\tilde{\mathbf{q}} = [m_c, n_c, 1]^T$ , since only  $\mathbf{q}_c$  is available, one way to get  $\mathbf{q}_v$  can be denoted by

$$\mathbf{q}_v = \begin{bmatrix} m_v \\ n_v \end{bmatrix} = \frac{1}{r_3\tilde{\mathbf{q}}} \begin{bmatrix} r_1\tilde{\mathbf{q}} \\ r_2\tilde{\mathbf{q}} \end{bmatrix}. \quad (6)$$

where the  $r_i \in \mathbb{R}^{1 \times 3}$  is the  $i$ th row of the matrix  ${}^V\mathbf{R}_C$ .

Now a circle-based image moment is considered to control the translation motion of the quadrotor, its  $2-D$  moments  $m_{ij}$  of order  $i + j$  are defined by:

$$m_{ij} = \iint m_v^i n_v^j dm_v dn_v,$$

The perspective moments are chosen as  $x_g = m_{10}/a$ ,  $y_g = m_{01}/a$ , and  $a = m_{00}$  being the circle area. Therefore, the image moment features are defined as

$$\mathbf{s}_t = [a_n x_g, a_n y_g, a_n]^T, \quad (7)$$

where  $a_n = \sqrt{a^*/a}$ , and  $a^*$  is its desired value of circle area, which can be calculated using the desired images.

The visual dynamics is presented for the visual servoing after simple computations as follows:

$$\dot{\mathbf{s}}_t = -\frac{1}{Z_V^*}(\mathbf{v} - \mathbf{v}_t). \quad (8)$$

where the  $Z_V^* > 0$  is its desired depth from  $\mathcal{V}$  to target plane.

*Remark 1:* The designed visual features  $\mathbf{s}_t$  are not dependent on a desired depth  $Z_V^*$ , and the derived visual dynamics (8) are very simple and decoupled. Compared with a discrete set of point features, a novel circle-based moment feature defined in a non-rotating virtual image plane has angle invariance and is more robust for the interference of untextured

or unreliable textures in practical scenes. As a result, the characteristics of visual dynamics are crucial to the design of the subsequent controller.

### C. Problem Statement

The objective of this work is to design a robust image-based controller for the landing of a low-cost quadrotor on an unpredictable moving vehicle. The unpredictable ground vehicle implies that there is not any prior model knowledge so that the linear velocity  $\mathbf{v}_t$  and the angular velocity  $\boldsymbol{\Omega}_t$  can't be measured or estimated in the closed-loop system. The quadrotor requires only a minimal sensing suit that is a monocular camera and an IMU, which can execute some interesting and real-time applications in GPS-denied environments, such as cities and forests. The target's linear velocity  $\mathbf{v}_t$  is only bounded but can be a time-varying configuration. Specifically, given a desired image moment  $\mathbf{s}_t^*$ , the goal is to design the thrust force  $f$  and the torque input  $\boldsymbol{\tau}$  for the quadrotor so that the designed visual feature converges to a predefined and arbitrarily small neighborhood of  $\mathbf{s}_t^*$ . More importantly, it implies that the quadrotor reaches the desired position relative to the moving vehicle in Cartesian space.

## III. CONTROL DESIGN

In this section, the design of the robust image-based controller is provided in detail. The landing controller involves a cascaded control paradigm, including an IBVS outer-loop controller to govern the translational motion, and a geometric inner-loop controller to regulate the rotational motion, as is shown in Fig. 3. Finally, the stability analysis is presented based on Lyapunov stability theory.

### A. Performance Funnel for Landing

Before designing the controller, we first introduce the concept of a performance funnel  $\mathcal{F}_\rho$ , which is constructed to shape the evolution of the error  $\mathbf{e}_i$  as

$$\mathcal{F}_\rho := \{(t, \mathbf{e}_i) \in \mathbb{R}_{\geq 0} \times \mathbb{R} \mid \|\mathbf{e}_i(t)\| < \rho_i(t)\}, \quad (9)$$

where  $\mathbb{R}_{\geq 0}$  denote the sets of nonnegative real numbers.

It is worth noting that the funnel boundary is flexible, and a monotone funnel is convenient to be chosen in most situations. A funnel function  $\rho_i(t)$  can be defined by the following exponentially decaying form

$$\rho_i(t) = (\rho_i(0) - \rho_i^\infty) \exp(-l_i t) + \rho_i^\infty. \quad (10)$$

where the  $\rho_i(0) > 0$  denotes a maximum allowable error; the constant  $l_i > 0$  represents the exponential convergence rate of the error;  $\rho_i^\infty > 0$  is the steady-state performance specification; They all are design parameters.

*Remark 2:* An important feature of the performance funnel boundary is that it is far away from zero and flexible, which allows the convergence residual set, convergence speed, and error overshoot to be determined in advance. To this end, a variety of different funnel boundaries is possible. Furthermore, the funnel function is introduced for the design of a robust IBVS controller.

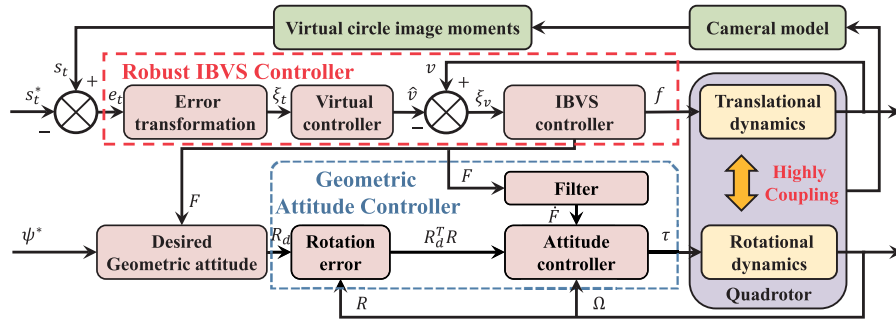


Fig. 3. Block diagram of the proposed robust landing controller for the underactuated quadrotor.

*Remark 3:* Owing to the flexibility properties of the performance funnel function, the initial maximum allowable error  $\rho_i(0)$  of the funnel function can be set quantitatively a priori based on the initial error  $e_i(0)$ . By designing a proper funnel function for landing tasks, the initial error is always within the boundaries, achieving the convergence of the feature errors to a predefined neighborhood of zero.

### B. Robust IBVS Controller Design

To begin with, the feature error is defined as  $e_t = s_t - s_t^*$ . Using the performance funnel functions, we can define the following image error transformation

$$\xi_{t,k} = e_{t,k} / \rho_{t,k}, \quad (11)$$

where  $e_{t,k}$  is  $k^{th}$  variable of  $e_t$ , for  $k = 1, 2, 3$ . As long as it is guaranteed that the boundary of the transformed error such that  $|\xi_{t,k}| \leq 1$ , the  $e_{t,k}$  can be enforced to remain strictly within the time-varying boundary of  $\rho_{t,k}$ ,  $\forall t \geq 0$ . Since the boundary of the performance funnel is flexible and completely self-designed, it meets the requirements of transient and steady-state performance for landing in many applications of interest.

The differentiation of (11) with respect to time is given by

$$\dot{\xi}_{t,k} = \frac{\dot{e}_{t,k} \rho_{t,k} - e_{t,k} \dot{\rho}_{t,k}}{\rho_{t,k}^2}. \quad (12)$$

To guarantee  $|\xi_{t,k}| \leq 1$ , the following log-type Barrier Lyapunov Function (BLF) candidate is employed due to its ability to provably establish invariance of sets by

$$V_t = \sum_{k=1}^3 \left( \frac{1}{2} \ln \frac{1}{1 - \xi_{t,k}^2} \right). \quad (13)$$

Exploiting (8), we can derive from (13) that

$$\dot{V}_t = \sum_{k=1}^3 \left[ \frac{\xi_{t,k}}{\rho_{t,k}(1 - \xi_{t,k}^2)} \left( -\frac{v_k - v_{t,k}}{Z_V^*} - \dot{\rho}_{t,k} \xi_{t,k} \right) \right]. \quad (14)$$

Define the velocity errors as  $e_{v,k} = v_k - \hat{v}_k$ , where  $\hat{v}_k$  is a virtual intermediate variable to be designed later. Then (14)

can be rewritten as

$$\begin{aligned} \dot{V}_t &= \sum_{k=1}^3 \left[ \frac{\xi_{t,k}}{\rho_{t,k}(1 - \xi_{t,k}^2)} \left( -\frac{v_k + \hat{v}_k - \hat{v}_k - v_{t,k}}{Z_V^*} - \dot{\rho}_{t,k} \xi_{t,k} \right) \right] \\ &= \sum_{k=1}^3 \left[ \frac{\xi_{t,k}}{\rho_{t,k}(1 - \xi_{t,k}^2)} \left( -\frac{e_{v,k} + \hat{v}_k - v_{t,k}}{Z_V^*} - \dot{\rho}_{t,k} \xi_{t,k} \right) \right]. \end{aligned}$$

To guarantee  $\xi_{t,k}$  is Lyapunov stable, the virtual intermediate variable  $\hat{v}_k$  is given by

$$\hat{v}_k = K_{t,k} \frac{e_{t,k}}{1 - \xi_{t,k}^2}, \quad (15)$$

where  $K_{t,k} > 0$  is a positive constant.

Similarly as (11) and (13), we get the transformed errors  $\xi_{v,k} = e_{v,k} / \rho_{v,k}$ , and the time-varying barrier function is constructed for the transformed velocity error as

$$V_v = \sum_{k=1}^3 \left( \frac{1}{2} \ln \frac{1}{1 - \xi_{v,k}^2} \right), \quad (16)$$

The time derivative of  $V_v$  gives

$$\dot{V}_v = \sum_{k=1}^3 \left[ \frac{\xi_{v,k}}{\rho_{v,k}(1 - \xi_{v,k}^2)} (\dot{e}_{v,k} - \dot{\rho}_{v,k} \xi_{v,k}) \right]. \quad (17)$$

Substituting (2) into (17), one yield

$$\dot{V}_v = \sum_{k=1}^3 \left[ \frac{\xi_{v,k}}{\rho_{v,k}(1 - \xi_{v,k}^2)} \left( \bar{g}_k - \frac{\bar{f}_k}{m} - \dot{v}_k - \dot{\rho}_{v,k} \xi_{v,k} \right) \right], \quad (18)$$

where  $\bar{g}_k$  is  $k^{th}$  variable of  $\bar{\mathbf{g}} = [0, 0, g]^T$ , and  $\bar{f}_k$  is  $k^{th}$  variable of  $\bar{\mathbf{f}} = \mathbf{f} \mathbf{R} \mathbf{i}_3$ . Now, the thrust  $f$  is designed as

$$f = \mathbf{F}^T (\mathbf{R} \mathbf{i}_3), \quad (19)$$

where  $F_k = m \bar{g}_k + K_{v,k} \frac{e_{v,k}}{1 - \xi_{v,k}^2}$  is  $k^{th}$  variable of  $\mathbf{F} \in \mathbb{R}^3$ , and  $K_{v,k} > 0$  is a constant for  $k = 1, 2, 3$ .

*Remark 4:* Several similar BLFs are effectively used to deal with the state constraints problem, mainly including tan-type and log-type. Based on the characteristic of the two kinds of functions, both of them are feasible to guarantee  $|\xi_{t,k}| \leq 1$ . Here we use a log-type BLF in the proposed method. However, notice that the highlight of the proposed method is not to design a novel barrier function, but to propose an error transformation based on funnel function for the IBVS control, thereby directly governing the performance

of errors in the image plane. Two BLFs are exploited to achieve tailored image features and linear velocity tracking performance at both transient and steady states, respectively. On the other hand, due to the properties of the BLF appearing in (13) and (16), it leads to proving that  $\xi_{t,k}$  and  $\xi_{v,k}$  evolve strictly within the open set  $(-1, 1)$ . As a result, the proposed landing scheme is of robustness due to the feature errors being strictly driven within the prescribed performance funnel. Therefore, it does not incorporate both the desired depth information of target features and any prior model knowledge of the moving vehicle. What's more, this control mechanism avoids the tedious algebra related to backstepping iterations and can be efficiently implemented on the low-cost quadrotor.

### C. Geometric Attitude Controller Design on SO(3)

The attitude controller is developed directly using rotation matrices to avoid the singularities of Euler-angles and the ambiguity of quaternions. In the following, the desired rotation matrices are defined by the geometric methods, and attitude error configuration on nonlinear manifolds SO(3) are presented to design the geometric attitude controller.

The desired attitude  $\mathbf{R}_d = [\mathbf{r}_{d1}, \mathbf{r}_{d2}, \mathbf{r}_{d3}]$  is directly extracted from  $\mathbf{F}$  as follows

$$\begin{cases} \mathbf{r}_{d1} = \mathbf{r}_{d2} \times \mathbf{r}_{d3}, \\ \mathbf{r}_{d2} = \frac{\mathbf{r}_{d3} \times \mathbf{b}}{\|\mathbf{r}_{d3} \times \mathbf{b}\|}, \\ \mathbf{r}_{d3} = -\frac{\mathbf{F}}{\|\mathbf{F}\|}, \end{cases} \quad (20)$$

where desired yaw angle vector  $\mathbf{b} = [\cos(\psi^*), \sin(\psi^*), 0]^T$ . Since the symmetrical physical structure of the quadrotor, only an arbitrarily fixed  $\psi^*$  is required when landing. To achieve  $\mathbf{R} \rightarrow \mathbf{R}_d$ , a real-valued error function is defined as

$$\Upsilon(\mathbf{R}, \mathbf{R}_d) = \frac{1}{2} \text{tr}[\mathbf{I} - \mathbf{R}_d^T \mathbf{R}]. \quad (21)$$

The attitude error is denoted in the sublevel set  $L = \{\mathbf{R} \in \text{SO}(3) \mid \Upsilon(\mathbf{R}, \mathbf{R}_d) < 2\}$ , which almost covers SO(3).

The desired angular velocity and its derivative are given by  $\Omega_d^\wedge = \mathbf{R}_d^T \dot{\mathbf{R}}_d$  and  $\dot{\Omega}_d^\wedge = (\Omega_d^\wedge)^T \mathbf{R}_d^T \dot{\mathbf{R}}_d + \mathbf{R}_d^T \ddot{\mathbf{R}}_d$ . The attitude and angular velocity errors are chosen as

$$\mathbf{e}_R = \frac{1}{2}(\mathbf{R}_d^T \mathbf{R} - \mathbf{R}^T \mathbf{R}_d)^\vee, \quad (22)$$

$$\mathbf{e}_\Omega = \Omega - \mathbf{R}^T \mathbf{R}_d \Omega_d. \quad (23)$$

Motivated by the standard geometric controller designed in [23], we design the torque input  $\boldsymbol{\tau}$  as follows,

$$\begin{aligned} \boldsymbol{\tau} = & -k_R \mathbf{e}_R - k_\Omega \mathbf{e}_\Omega + \Omega^\wedge \mathbf{J} \Omega \\ & - \mathbf{J}(\Omega^\vee \mathbf{R}_d^T \mathbf{R} \Omega_d - \mathbf{R}^T \mathbf{R}_d \dot{\Omega}_d). \end{aligned} \quad (24)$$

where  $k_R, k_\Omega$  are positive constant gains.

### D. Stability Analysis

Consider the proposed outer-loop IBVS controller (19) and inner-loop geometric controller (24), the corresponding stability results can be stated in the following claim:

**Theorem 1:** For the image-based landing system introduced in (1)-(4) and (8), all closed-loop signals are uniformly ultimately bounded, and the transient and steady-state performance of errors are guaranteed within the funnel function (10).

*Proof:* To analyze the stability of the rotational error dynamics, differentiating equations (21) and (23) and substituting (24) into (4), we have:

$$\dot{\Upsilon}(\mathbf{R}, \mathbf{R}_d) = \mathbf{e}_R^T \mathbf{e}_\Omega, \quad (25)$$

$$\mathbf{J} \dot{\mathbf{e}}_\Omega = -k_R \mathbf{e}_R - k_\Omega \mathbf{e}_\Omega, \quad (26)$$

Consider the following Lyapunov candidate function as

$$\mathbf{V} = \frac{1}{2} \mathbf{e}_\Omega^T \mathbf{J} \mathbf{e}_\Omega + k_R \Upsilon(\mathbf{R}, \mathbf{R}_d), \quad (27)$$

Then the time derivative of  $\mathbf{V}$  is

$$\dot{\mathbf{V}} = \mathbf{e}_\Omega^T \mathbf{J} \dot{\mathbf{e}}_\Omega + k_R \mathbf{e}_R^T \mathbf{e}_\Omega = -k_\Omega \|\mathbf{e}_\Omega\|^2 \leq 0. \quad (28)$$

Based on the Lyapunov stability theory, we have  $\mathbf{e}_\Omega \rightarrow 0$  when  $t \rightarrow \infty$  since  $\dot{\mathbf{V}} \leq 0$ . Moreover, it can be shown that the  $\dot{\mathbf{e}}_\Omega$  is uniformly continuous. Applying Barbalat's Lemma to (26), it follows that  $\dot{\mathbf{e}}_\Omega \rightarrow 0$  as  $t \rightarrow \infty$ . Then  $\mathbf{e}_R \rightarrow 0$  when  $t \rightarrow \infty$ . Therefore, the attitude controller achieves asymptotic stability for rotational error dynamics.

To prove the stability of the overall translational error dynamics, it suffices to show the transformed errors  $\xi_{t,k}$  and  $\xi_{v,k}$  are bounded within the open set  $(-1, 1)$ . Therefore, we can further demonstrate  $e_{t,k}$  and  $e_{v,k}$  achieve the pre-determined performance specified by (10). In the following, we proceed in three steps to prove the stability. In step 1, the existence and uniqueness of a maximal system solution  $[\xi_{t,k}, \xi_{v,k}]^T: [0, \tau_{max}) \rightarrow \mathbf{A}_\xi$  for some  $\tau_{max} > 0$ , is guaranteed. In step 2, the boundedness of all closed-loop signals is proven, and their boundaries belong to a compact subset of  $\mathbf{A}_\xi$ . Consequently, in step 3, the points raised in the second step are proven to remain when  $\tau_{max} \rightarrow \infty$ .

**Step 1:** Prove the existence and uniqueness of the system solution over a time interval  $[0, \tau_{max})$ .

An open set is first defined as

$$\mathbf{A}_\xi = (-1, 1) \times (-1, 1). \quad (29)$$

The set  $\mathbf{A}_\xi$  is nonempty and open. Using (10), the fact that constructed funnel function satisfies  $\|\rho_{t,k}(0)\| > \|e_{t,k}(0)\|$  and  $\|\rho_{v,k}(0)\| > \|e_{v,k}(0)\|$ , therefore the  $\|\xi_{t,k}(0)\| = \|e_{t,k}(0)/\rho_{t,k}(0)\| < 1$  and  $\|\xi_{v,k}(0)\| = \|e_{v,k}(0)/\rho_{v,k}(0)\| < 1$ . If we define  $\xi_k = [\xi_{t,k}, \xi_{v,k}]^T$ , where  $k = 1, 2, 3$ . As a result, the  $\xi_k \in \mathbf{A}_\xi$ . The time derivative of  $\xi_k$  is given by

$$\dot{\xi}_k = \begin{bmatrix} \frac{1}{\rho_{t,k}} \left( \frac{\dot{e}_{t,k}}{\rho_{t,k}} - \xi_{t,k} \dot{\rho}_{t,k} \right) \\ \frac{1}{\rho_{v,k}} \left( \frac{\dot{e}_{v,k}}{\rho_{v,k}} - \xi_{v,k} \dot{\rho}_{v,k} \right) \end{bmatrix}. \quad (30)$$

Since funnel functions  $\rho_{t,k}$  and  $\rho_{v,k}$  are bounded by construction, the  $\dot{\rho}_{t,k}$ ,  $\xi_{t,k}$ ,  $\dot{\rho}_{v,k}$ , and  $\xi_{v,k}$  are bounded and continuously differentiable with time. Utilizing (15) and (19), the intermediate control signal  $\hat{\mathbf{v}}$  and control law  $f$  are smooth over  $\mathbf{A}_\xi$ , then  $\dot{e}_{t,k}$  and  $\dot{e}_{v,k}$  are continuously differentiable functions. Therefore  $\dot{\xi}_k$  is bounded and continuously differentiable as well as locally Lipschitz  $\xi_k$  over the set  $\mathbf{A}_\xi$ . Thus, a uniqueness

of a maximal solution  $\xi_k: [0, \tau_{max}) \rightarrow A_\xi$  of  $\dot{\xi}_k$  over the set  $A_\xi$  for a time interval  $[0, \tau_{max})$  is guaranteed, which implies

$$\xi_{t,k} \in (-1, 1), \quad \zeta_{v,k} \in (-1, 1), \quad \forall t \in [0, \tau_{max}). \quad (31)$$

**Step 2:** The boundedness of all closed-loop signals is proven, and their boundaries belong to a compact subset of  $A_\xi$  for all  $t \in [0, \tau_{max})$ .

Substituting the (15) into (14), we have

$$\dot{V}_t = - \sum_{k=1}^3 \frac{K_{t,k}}{Z_V^*} \frac{\xi_{t,k}^2}{(1 - \xi_{t,k}^2)^2} + \sum_{k=1}^3 \frac{\xi_{t,k}}{\rho_{t,k}(1 - \xi_{t,k}^2)} \kappa_{t,k}, \quad (32)$$

where  $\kappa_{t,k} = -e_{v,k} + v_{t,k} - \dot{\rho}_{t,k} \xi_{t,k}$ .

Since chosen functions  $\rho_{t,k} > 0$ ,  $\rho_{v,k} > 0$ ,  $\dot{\rho}_{t,k}$ , and  $\dot{\rho}_{v,k}$  are bounded, one observes the  $e_{v,k} = \rho_{v,k} \xi_{v,k}$  is bound. Under Assumption 1, the linear velocity of vehicle  $v_{t,k}$  is bounded. Additionally, we can conclude that the boundedness of  $\kappa_{t,k}$  for all  $t \in [0, \tau_{max})$  such that

$$\|\kappa_{t,k}\| \leq \|e_{v,k}\| + \|v_{t,k}\| + \|\dot{\rho}_{t,k} \xi_{t,k}\| \leq \Delta_{t,k}, \quad (33)$$

Because  $\rho_{t,k} > \rho_\infty^{t,k} > 0$ , it exists  $1/\rho_{t,k} \leq \epsilon_{t,k}$ , and the following inequality holds in terms of Young's inequality

$$\frac{\xi_{t,k}}{\rho_{t,k}(1 - \xi_{t,k}^2)} \kappa_{t,k} \leq \frac{\sigma_{t,k} \xi_{t,k}^2}{(1 - \xi_{t,k}^2)^2} + \frac{\epsilon_{t,k}}{4\sigma_{t,k}} \Delta_{t,k}^2, \quad (34)$$

where  $\sigma_{t,k}$  is a positive constant.

Noting that  $\xi_{t,k} \in (-1, 1)$  for all  $t \in [0, \tau_{max})$  in (31), we get  $1/(1 - \xi_{t,k}^2) \geq 1, \forall t \in [0, \tau_{max})$ . Using [39], the following inequality holds

$$\frac{\xi_{t,k}^2}{(1 - \xi_{t,k}^2)^2} \geq \frac{\xi_{t,k}^2}{1 - \xi_{t,k}^2} \geq \ln \frac{1}{1 - \xi_{t,k}^2}, \quad (35)$$

Therefore, the inequality (32) can be represented as

$$\dot{V}_t \leq -a_t V_t + b_t, \quad (36)$$

where  $a_t = \min(K_{t,k}/Z_V^* - \sigma_{t,k}, |k = 1, 2, 3)$ , and  $b_t = \sum_{k=1}^3 \epsilon_{t,k} \Delta_{t,k}^2 / (4\sigma_{t,k})$ . We assume that  $K_{t,k}$  and  $\sigma_{t,k}$  are chosen as  $K_{t,k}/Z_V^* > \sigma_{t,k}$  such that  $-a_t < 0$ .

Integrating (36) over  $t \in [0, \tau_{max})$  yields

$$0 \leq V_t(t) \leq V_t(0)e^{-a_t} + b_t/a_t. \quad (37)$$

Obviously, we can conclude the terms  $\ln[1/(1 - \xi_{t,k}^2)]$  is bounded such that  $-1 < \underline{\xi}_{t,k} < \xi_{t,k} < \bar{\xi}_{t,k} < 1, \forall t \in [0, \tau_{max})$  for all  $k \in 1, 2, 3$ .

Review the (18), we have

$$\dot{V}_v = \sum_{k=1}^3 \left[ \frac{\xi_{v,k}^2}{\rho_{v,k}(1 - \xi_{v,k}^2)} (\bar{g}_k - \frac{F_k}{m} - \frac{\delta_k}{m} - \dot{v}_k - \dot{\rho}_{v,k} \xi_{v,k}) \right],$$

where  $\delta_k = \bar{f}_k - F_k$  is  $k$ th variable of the coupled term  $\delta = \bar{f} - F$ . Exploiting (20), the coupled term  $\delta$  between translational dynamics and rotational dynamics can be rewritten as

$$\delta = \|F\|(((R_d i_3)^T R i_3) R i_3 - R_d i_3). \quad (38)$$

According to Rodrigues' formula, we obtain  $\|e_R\| = \sin \|x\|$ , when  $R_d^T R = \exp \hat{x}$  for  $x \in \mathbb{R}^3$ , so  $\|e_R\|$  represents the sine of the eigen-axis rotation angle between  $R$  and  $R_d$  such that

$$\|(((R_d i_3)^T R i_3) R i_3 - R_d i_3)\| \leq \|e_R\| < 1. \quad (39)$$

Therefore we get  $\|\delta\| \leq \|F\|$ . From (18), yields

$$\|F_k\| \leq \|m \bar{g}_k\| + \|K_{v,k} \frac{e_{v,k}}{1 - \xi_{v,k}^2}\|. \quad (40)$$

Next, based on the designed thrust input (19), we have

$$\dot{V}_v = - \sum_{k=1}^3 \frac{K_{v,k}}{m} \frac{\xi_{v,k}^2}{(1 - \xi_{v,k}^2)^2} + \sum_{k=1}^3 \frac{\xi_{v,k}}{\rho_{v,k}(1 - \xi_{v,k}^2)} \kappa_{v,k}, \quad (41)$$

where  $\kappa_{v,k} = \frac{\delta_k}{m} - \dot{v}_k - \dot{\rho}_{v,k} \xi_{v,k}$ . Using (15), the time derivative of the virtual velocity is expressed as

$$\dot{v}_k = K_{t,k} \left[ \frac{\dot{e}_{t,k}}{(1 - \xi_{t,k}^2)^2} + \frac{2e_{t,k} \xi_{t,k} \dot{\xi}_{t,k}}{(1 - \xi_{v,k}^2)^2} \right]. \quad (42)$$

Since the fact that terms  $\|\xi_{t,k}\| < 1$ ,  $\|\xi_{v,k}\| < 1$ ,  $e_{t,k} = \rho_{t,k} \xi_{t,k}$ , and  $e_{v,k} = \rho_{v,k} \xi_{v,k}$  are bounded for all  $t \in [0, \tau_{max})$ , and the  $\dot{e}_{t,k}$  and  $\dot{\xi}_{t,k}$  are bounded in (36), then the  $\delta_k$  and  $\dot{v}_k$  are bounded such that the following inequality holds

$$\|\kappa_{v,k}\| \leq \frac{\|\delta_k\|}{m} + \|\dot{v}_k\| + \|\dot{\rho}_{v,k} \xi_{v,k}\| \leq \Delta_{v,k}. \quad (43)$$

Using  $1/\rho_{v,k} \leq \epsilon_{v,k}$  and Young's inequality, we have

$$\frac{\xi_{v,k}}{\rho_{v,k}(1 - \xi_{v,k}^2)} \kappa_{v,k} \leq \frac{\sigma_{v,k} \xi_{v,k}^2}{(1 - \xi_{v,k}^2)^2} + \frac{\epsilon_{v,k}}{4\sigma_{v,k}} \Delta_{v,k}^2, \quad (44)$$

where  $\sigma_{v,k}$  is a positive constant. Because of (35), (38) is written as follows,

$$\dot{V}_v \leq -a_v V_v + b_v, \quad (45)$$

where  $a_v = \min(K_{v,k}/m - \sigma_{v,k}, |k = 1, 2, 3)$ , and  $b_v = \sum_{k=1}^3 \epsilon_{v,k} \Delta_{v,k}^2 / (4\sigma_{v,k})$ . We assume that  $K_{v,k}$  and  $\sigma_{v,k}$  are chosen as  $K_{v,k}/m > \sigma_{v,k}$  such that  $-a_v < 0$ .

Integrating (45) over  $t \in [0, \tau_{max})$  yields

$$0 \leq V_v(t) \leq V_v(0)e^{-a_v} + b_v/a_v. \quad (46)$$

So the terms  $\ln[1/(1 - \xi_{v,k}^2)]$  is bounded such that  $-1 < \underline{\xi}_{v,k} < \xi_{v,k} < \bar{\xi}_{v,k} < 1, \forall t \in [0, \tau_{max})$ . From the previous discussion, all signals are uniformly ultimately bounded for all  $t \in [0, \tau_{max})$ .

**Step 3:** The points raised in the second part are proven to remain when  $\tau_{max} \rightarrow \infty$ .

It is verified that  $\xi_j(t) \in A'_\xi$  for all  $t \in [0, \tau_{max})$ , where the set  $A'_\xi = (\underline{\xi}_{pj}, \bar{\xi}_{pj}) \times (\underline{\xi}_{vj}, \bar{\xi}_{vj}) \in A_\xi$  is nonempty and compact. However [45] dictates the existence of a time instant  $t' \in [0, \tau_{max})$  such that  $\xi_j(t') \notin A'_\xi$ . Thus we naturally come to the conclusion that  $\tau_{max} = \infty$  by contradiction, and completes the proof. ■



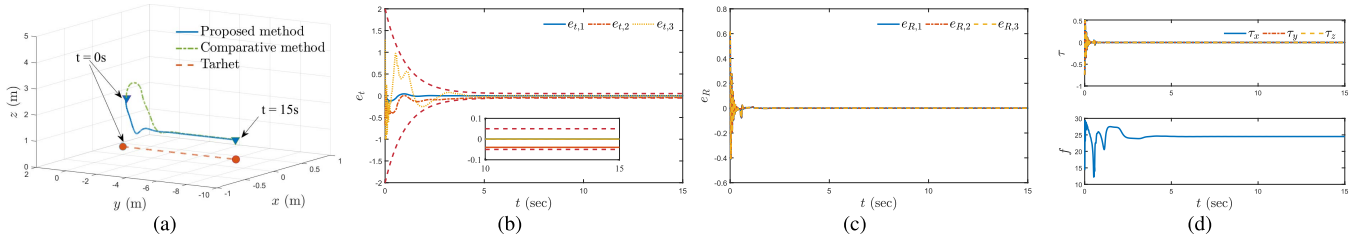


Fig. 4. The comparative study for the proposed virtual circle image moments and the classical spherical image moments. (a) Trajectories of a quadrotor and a moving target. (b) The evolution of the image feature errors along with the corresponding funnel boundaries (red). (c) The time response of attitude errors  $e_R = [e_{R,1}, e_{R,2}, e_{R,3}]^T$ . (d) The torque inputs  $\tau = [\tau_x, \tau_y, \tau_z]^T$  and net thrust force  $f$  of the quadrotor with respect to time.

### E. Modified Geometric Attitude Controller Based on Filter

From a practical standpoint, it is possible to neglect the last two terms in the controller and achieve satisfactory performance [1]. Especially, this method has been adopted in the standard PX4 controller [46]. In addition, [47] have presented that the geometric controller remains stable in the absence of the higher-order inertial cancellation terms when the desired attitude is fixed. Therefore, the higher-order inertial cancellation terms are neglected for the fixed desired attitude, and the geometric attitude control law is given by

$$\tau = -k_R e_R - K_\Omega e_\Omega + \Omega^\wedge J \Omega. \quad (47)$$

*Remark 5:* There is no doubt that the controller (47) is effective but suffers from the disadvantage of needing the target velocity measurements  $v_t$ . This is because  $\Omega_d$  implemented in  $e_\Omega$  depends on the derivative of the quadrotor thrust  $\dot{F}$ , and  $\dot{F}$  is related to  $v_t$ . However, since the velocity of the unpredictable moving target is unavailable,  $\dot{F}$  can't be obtained (hence the desired angular velocity  $\Omega_d$  can't be defined). To avoid the velocity measurements for unpredictable targets, a command filter is designed to obtain  $\dot{F}$  so that the desired angular velocity can be well-defined.

To eliminate the influence of unavailable velocity for  $\Omega_d$ , a command filter [48] is used herein to compute  $\dot{F}$  due to it requires that only the signal  $F$  and obviates the need for analytic computation of command signal derivatives as follows

$$\begin{cases} \dot{z}_{i,1} = \omega_n z_{i,2}, \\ \dot{z}_{i,2} = -2\zeta \omega_n z_{i,2} - \omega_n (z_{i,1} - F_i), \end{cases} \quad (48)$$

with  $i \in 1, 2, 3$ , and the outputs of each command filter denote  $z_{i,1} = F_i$  and  $z_{i,2} = \dot{F}_i$ . The parameters of filter can be chosen as  $\omega_n > 0$  and  $\zeta \in (0, 1]$ .

## IV. SIMULATIONS AND EXPERIMENTS

In this section, the theoretical results presented above are validated by simulation studies and experiments. No prior knowledge of ground vehicles is provided. We considered a circle with a radius of 0.08 m attached to the plane of the vehicle for visual servoing. The rotation matrix was initialized as  $R(0) = I$ . The desired image moments were set as  $s_t^* = [0, 0, 1]^T$ . The parameters of the quadrotor dynamics were set as follows:  $m = 2.48$  kg,  $g = 9.81$  m/s<sup>2</sup>, and  $J = \text{diag}(0.0756, 0.0756, 0.1277)$  kg · m<sup>2</sup>/rad<sup>2</sup>. The parameters of the controller were chosen for the repeatability results for both

simulation and experiment as follows:  $K_{t,1} = K_{t,2} = 4.5$ ,  $K_{t,3} = 2.25$ ,  $K_{v,1} = K_{v,2} = 2.5$ ,  $K_{v,3} = 1.25$ ,  $k_R = 20$ , and  $k_\Omega = 5$ . In addition, the gains of the filter (48) were chosen as  $\zeta = 0.5$  and  $\omega_n = 0.02$ . Before investigating experimental results using hardware, the simulation results allow us to gain insight into the proposed method in different scenarios that may be of a larger scale than it is possible in the hardware setup, e.g. due to restrictions regarding laboratory size.

### A. Simulation Results Considering a Comparative Study

Under the same simulation conditions, we evaluated the proposed IBVS controller defined in (19) and compared the results with those of the approach based on spherical image moments in [29]. The landing scheme in [29] is similarly defined for the system modeled by (1)-(4), but its controller requires the velocity of the target. In this simulation, the linear velocity of the vehicle was set as  $v_t = 0.5$  m/s, and the parameters of funnel function were given by  $\rho_{t,k}^\infty = 0.05$ ,  $\rho_{v,k}^\infty = 0.2$ , and  $l_{t,k} = l_{v,k} = 1$  for  $k = 1, 2, 3$ . The simulation results are shown in Fig. 4. Fig. 4(a) depicts the quadrotor's trajectories of the proposed method (blue) and the comparative method (green). The time evolution of the feature errors is illustrated in Fig. 4(b). The time evolution of the attitude errors is illustrated in Fig. 4(c). Fig. 4(d) shows the torque inputs  $\tau$  and net thrust force  $f$ . It can be observed that the trajectory of the quadrotor of the comparative method is not satisfactory due to the undesired behavior in the vertical axis. What's more, its convergence speed is slow. In contrary, the proposed method can guarantee the image feature errors converge to the neighborhood of zero without violating the designed funnels. Hence, the camera visibility and the transient and steady-state behaviors are potentially improved. Consequently, the results show the effectiveness of the proposed IBVS scheme although in the absence of the target velocity measurements.

### B. Simulation Results for Strong Robustness Verification

To further demonstrate the performance and robustness of the proposed landing controllers for practical applications. The quadrotor is considered to suffer from sensor noises and external disturbances. What's more, the target is endowed with complex motions involving acceleration and deceleration. Without loss of generality, the wind caused a time-varying accelerated speed disturbance as  $0.2 \sin(0.1t)$  m/s<sup>2</sup>; the noise was imposed on the normalized image feature measurements



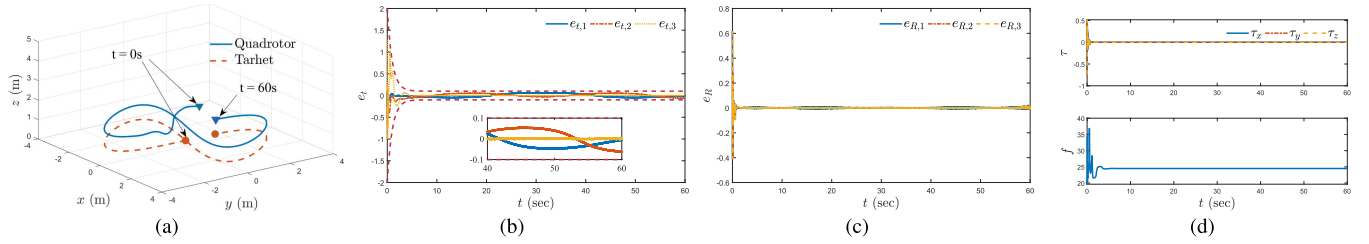


Fig. 5. Simulation results for the strong robustness verification, where the quadrotor landed on a target moving in an “8” shaped trajectory in a wind disturbance environment. (a) Trajectories of a quadrotor and a moving target. (b) The evolution of the image feature errors along with the corresponding funnel boundaries (red). (c) The time response of attitude errors. (d) The torque inputs and net thrust force of the quadrotor.

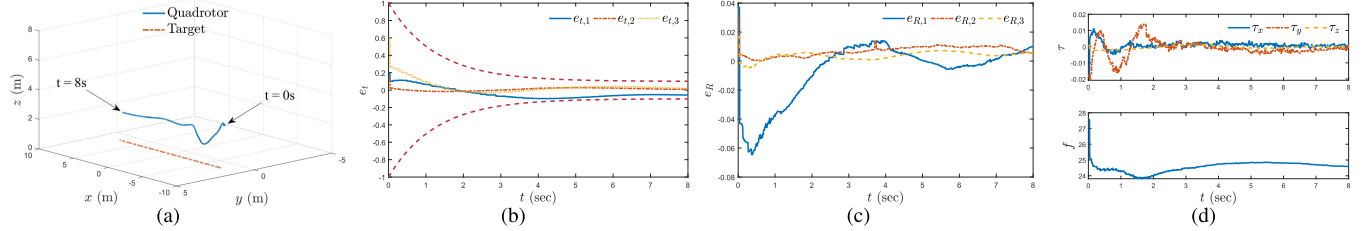


Fig. 6. Simulation in Gazebo: Quadrotor lands on a high-speed target moving in a linear trajectory (2m/s). (a) Trajectories of a quadrotor and a moving target. (b) The evolution of the image feature errors along with the corresponding funnel boundaries (red). (c) The time response of attitude errors. (d) The torque inputs and net thrust force of the quadrotor.

with a standard deviation of 0.005; an “8” shaped motion trajectory was chosen as

$$\begin{cases} \dot{x}_t = v_t \cos(\theta_t), & \dot{y}_t = v_t \sin(\theta_t), & \dot{\theta}_t = \Omega_t, \\ v_t = \sqrt{(0.3 \cos(0.1t))^2 + (0.4 \cos(0.2t))^2}, \\ \Omega_t = \frac{-0.024 \sin(0.2t) \cos(0.1t) - 0.12 \sin(0.1t) \cos(0.2t)}{v_t^2}, \end{cases}$$

where  $x_t$ ,  $y_t$ , and  $\theta_t$  denote the position and angle of the vehicle, respectively. The parameters of the funnel function were given by  $\rho_{t,k}^\infty = 0.1$ ,  $\rho_{v,k}^\infty = 0.2$ , and  $l_{t,k} = l_{v,k} = 1$  for  $k = 1, 2, 3$ . The results are shown in Fig. 5. Fig. 5(a) depicts the trajectories of a quadrotor and a moving target. The time evolution of the feature errors is plotted in Fig. 5(b). The time evolution of the attitude errors is illustrated in Fig. 5(c). Fig. 5(d) illustrates the torque inputs and net thrust force. It can be observed that the frequent variations of target velocities arose certain tracking errors, the noise imposed negative influences on image feature measurements and the wind caused a time-varying accelerated speed disturbance. However, the quadrotor can track the moving target with a smooth trajectory. This part is due to that the image feature errors are strictly driven within the prescribed performance funnel. Therefore, the studies show the strong robustness of the proposed method although in the presence of sensor noises, external disturbances, and complex target trajectories.

### C. Simulation in GAZEBO for the High-Speed Targets

There is no doubt that the high-speed targets are important in practice. To evaluate the performance for a high-speed target, we further test the control algorithm using Gazebo virtual world and robot operating system (ROS). The Gazebo allows simulation of robotic and sensors applications in almost real three-dimensional indoor and outdoor environments results so

that the simulation algorithms can be directly deployed to the real robot hardware. The velocity of the high-speed target was given by  $v_t = 2$  m/s. The parameters of funnel function were given by  $\rho_{t,k}^\infty = 0.2$ ,  $\rho_{v,k}^\infty = 0.3$ , and  $l_{t,k} = l_{v,k} = 0.8$  for  $k = 1, 2, 3$ . The results are shown in Fig. 6. Fig. 6(a) illustrates the trajectories of a quadrotor and a high-speed target. Fig. 6(b) and Fig. 6(c) depict the time response of feature errors and attitude errors. Fig. 6(d) shows the torque inputs  $\tau$  and net thrust force  $f$ . From the results, although the high-speed target arose certain tracking errors, the image feature errors still satisfied the transient and steady-state specifications imposed by the corresponding performance funnel. More significantly, the proposed method can be adapted to the different high-speed targets due to the fact that it can freely select the performance boundary. But in addition to this extreme requirement, a fixed satisfying performance boundary is enough to handle most low-speed scenarios. As a result, a quadrotor can track a high-speed target effectively and the landing trajectory is satisfactory. From this study, the effectiveness of the proposed method for a high-speed target is demonstrated.

### D. Experimental Results

In addition to the simulation study, we further test the proposed control method in a real-world experiment on the quadrotor developed in our Robotic Laboratory. As shown in Fig. 7, the entire experimental platform includes a quadrotor with a down-looking monocular camera and a mobile robot Husky attached a circle mark. The DAHENG IMAGI NG VEN-161 as a monocular camera is used to get its grayscale image at 50 Hz. The quadrotor is equipped with an open-source autopilot Pixhawk 4 (building-in IMUs) for the control purpose, and the algorithm was implemented on an onboard computer that communicates with Pixhawk 4 via

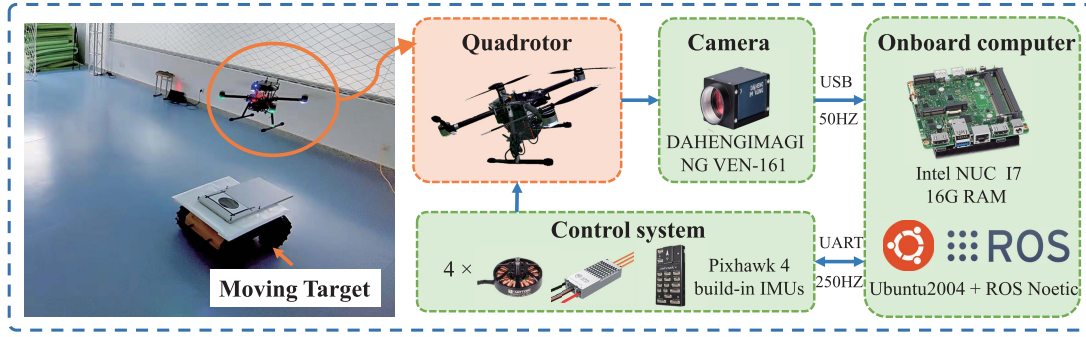


Fig. 7. The overall experiment setup for the landing system.

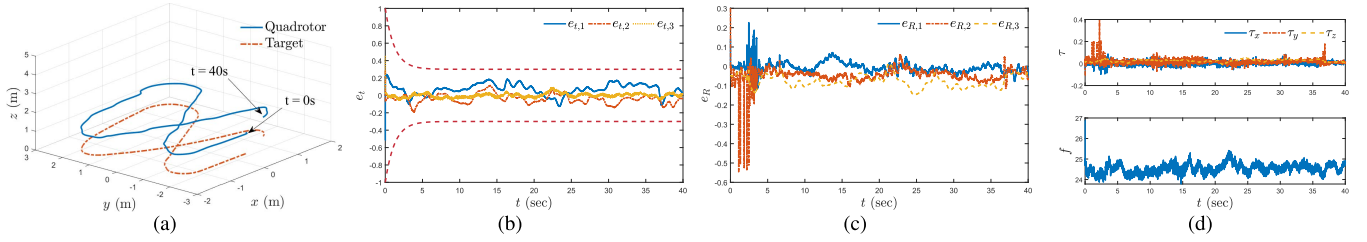


Fig. 8. Experiment 1: Quadrotor lands on an unpredictable moving target moving in an “8” shape trajectory. (a) Trajectories of a quadrotor and a moving target. (b) The evolution of the image feature errors along with the corresponding funnel boundaries (red). (c) The time response of attitude errors. (d) The torque inputs and net thrust force of the quadrotor.

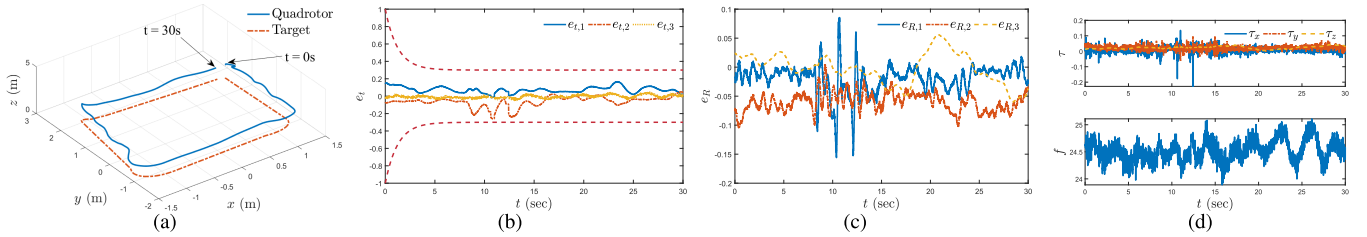


Fig. 9. Experiment 2: Quadrotor lands on an unpredictable moving target moving in a rectangular trajectory. (a) Trajectories of a quadrotor and a moving target. (b) The evolution of the image feature errors along with the corresponding funnel boundaries (red). (c) The time response of attitude errors. (d) The torque inputs and net thrust force of the quadrotor.

MAVROS protocol. Using the native topics of MAVROS named “mavros/actuator\_control,” we can send raw servo values to Pixhawk 4 for direct actuator controls. The essential thing is that the thrust and torque, designed in Eq. (19) and Eq. (48), have to be published in a normalized form. The image processing algorithm, and the image-based landing control law are directly implemented on the Intel NUC i7 PC onboard the quadrotor. The feedback control loop runs at a frequency of about 250 Hz. The proposed algorithm is implemented in the robot operating system neotic, running on Ubuntu 20.04. The parameters of funnel function were set as  $\rho_{t,k}^{\infty} = 0.3$ ,  $\rho_{v,k}^{\infty} = 0.5$ , and  $l_{t,k} = l_{v,k} = 0.8$  for  $k = 1, 2, 3$ . The OptiTrack motion capture system is only utilized to obtain the ground truth information about the 3-D positions of the quadrotor and target with respect to the global coordinate frame. Two cases of experiments were considered as follows:

*Case 1:* The target moves in an “8” shaped trajectory.

*Case 2:* The target moves in a rectangular trajectory.

In the first case, the quadrotor was required to track a moving target moving in an “8” shaped trajectory. The

experimental results are shown in Fig. 8. Fig. 8(a) illustrates the trajectories of a quadrotor and a landing vehicle recorded by the OptiTrack system. The time evolution of the feature errors is plotted in Fig. 8(b). The time evolution of the attitude errors is illustrated in Fig. 8(c). Fig. 8(d) shows the torque inputs  $\tau$  and net thrust force  $f$ . It can be observed the quadrotor follows the unpredictable moving target effectively, and the image feature errors converge to a neighborhood around zero without violation of the prescribed transient bound. The results show the effectiveness of the proposed IBVS scheme.

In the second case, the quadrotor was required to track a moving target moving in a rectangular trajectory. The results are shown in Fig. 9. Fig. 9(a) indicates the tracking trajectory. The time evolution of the feature errors is plotted in Fig. 9(b). The time evolution of the attitude errors is illustrated in Fig. 9(c). Fig. 9(d) shows the torque inputs and net thrust force. It can be observed that the image feature errors are strictly retained within performance funnels. Therefore, the quadrotor attained the smooth tracking trajectory for landing although in the absence of the velocity information of the

target. The experimental results verify that the quadrotor can track the target quickly and has a good tracking performance, which further exhibit the performance of the proposed method.

## V. CONCLUSION

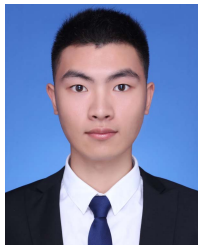
In this paper, a robust IBVS controller has been designed to land a quadrotor on an unpredictable moving vehicle using a circle feature. In particular, the passivity-like property of the circle features was preserved by reprojecting to the virtual image plane. By designing the error transformation in image space, the proposed IBVS controller can overcome the lack of both the desired depth information of the features and the velocity measurements of the targets. The proposed geometric attitude controller could cope with unpredictable moving target because the desired angular velocity was obtained by a command filter. The stability of the landing control scheme was proved using Lyapunov stability theory on a cascaded system. Simulation studies and experiment results have demonstrated the effectiveness of the proposed controller. In the future work, we plan to extend the proposed strategy to situations where cameras have visibility constraints.

## REFERENCES

- [1] V. Kumar and N. Michael, "Opportunities and challenges with autonomous micro aerial vehicles," *Int. J. Robot. Res.*, vol. 31, no. 11, pp. 1279–1291, 2012.
- [2] D. Floreano and R. J. Wood, "Science, technology and the future of small autonomous drones," *Nature*, vol. 521, no. 7553, pp. 460–466, 2015.
- [3] N. Mathew, S. L. Smith, and S. L. Waslander, "Planning paths for package delivery in heterogeneous multirobot teams," *IEEE Trans. Autom. Sci. Eng.*, vol. 12, no. 4, pp. 1298–1308, Oct. 2015.
- [4] T. Ryan and H. J. Kim, "LMI-based gain synthesis for simple robust quadrotor control," *IEEE Trans. Autom. Sci. Eng.*, vol. 10, no. 4, pp. 1173–1178, Oct. 2013.
- [5] S. Grzonka, G. Grisetti, and W. Burgard, "A fully autonomous indoor quadrotor," *IEEE Trans. Robot.*, vol. 28, no. 1, pp. 90–100, Feb. 2012.
- [6] S.-R. Oh, K. Pathak, S. K. Agrawal, H. R. Pota, and M. Garratt, "Approaches for a tether-guided landing of an autonomous helicopter," *IEEE Trans. Robot.*, vol. 22, no. 3, pp. 536–544, Jun. 2006.
- [7] J. Dougherty, D. Lee, and T. Lee, "Laser-based guidance of a quadrotor uav for precise landing on an inclined surface," in *Proc. Amer. Control Conf.*, Jun. 2014, pp. 1210–1215.
- [8] B. J. Guerreiro, C. Silvestre, R. Cunha, and D. Cabecinhas, "LiDAR-based control of autonomous rotorcraft for the inspection of pier-like structures," *IEEE Trans. Control Syst. Technol.*, vol. 26, no. 4, pp. 1430–1438, Jul. 2017.
- [9] H. Wang, D. Zheng, J. Wang, W. Chen, and J. Yuan, "Ego-motion estimation of a quadrotor based on nonlinear observer," *IEEE/ASME Trans. Mechatronics*, vol. 23, no. 3, pp. 1138–1147, Jun. 2018.
- [10] A. Huster, "Relative position sensing by fusion monocular vision and inertial rate sensors," Ph.D. thesis, Stanford University, Stanford, CA, USA, 2003.
- [11] K. Zhang, F. Chaumette, and J. Chen, "Trifocal tensor-based 6-DOF visual servoing," *Int. J. Robot. Res.*, vol. 38, nos. 10–11, pp. 1208–1228, Sep. 2019.
- [12] G. Li, B. Gabrich, D. Saldana, J. Das, V. Kumar, and M. Yim, "ModQuad-vi: A vision-based self-assembling modular quadrotor," in *Proc. Int. Conf. Robot. Autom. (ICRA)*, May 2019, pp. 346–352.
- [13] K. P. Jain, M. Park, and M. W. Mueller, "Docking two multirotors in midair using relative vision measurements," 2020, *arXiv:2011.05565*.
- [14] A. Paris, B. T. Lopez, and J. P. How, "Dynamic landing of an autonomous quadrotor on a moving platform in turbulent wind conditions," in *Proc. IEEE Int. Conf. Robot. Autom. (ICRA)*, May 2020, pp. 9577–9583.
- [15] J. Lin, Y. Wang, Z. Miao, H. Zhong, and R. Fierro, "Low-complexity control for vision-based landing of quadrotor UAV on unknown moving platform," *IEEE Trans. Ind. Informat.*, vol. 18, no. 8, pp. 5348–5358, Aug. 2022.
- [16] A. Borowczyk, D.-T. Nguyen, A. P.-V. Nguyen, D. Q. Nguyen, D. Saussie, and J. Le Ny, "Autonomous landing of a multirotor micro air vehicle on a high velocity ground vehicle," *IFAC-PapersOnLine*, vol. 50, no. 1, pp. 10488–10494, 2017.
- [17] T. Baca *et al.*, "Autonomous landing on a moving vehicle with an unmanned aerial vehicle," *J. Field Robot.*, vol. 36, no. 5, pp. 874–891, 2019.
- [18] J. Ghommam and M. Saad, "Autonomous landing of a quadrotor on a moving platform," *IEEE Trans. Aerosp. Electron. Syst.*, vol. 53, no. 3, pp. 1504–1519, Jun. 2017.
- [19] F. Chaumette and S. Hutchinson, "Visual servo control. I. Basic approaches," *IEEE Robot. Autom. Mag.*, vol. 13, no. 4, pp. 82–90, Dec. 2006.
- [20] X. Li, H. Zhao, and H. Ding, "Logarithmic observation of feature depth for image-based visual servoing," *IEEE Trans. Autom. Sci. Eng.*, early access, Nov. 12, 2021, doi: [10.1109/TASE.2021.3125698](https://doi.org/10.1109/TASE.2021.3125698).
- [21] T. Xu, Y. Guan, J. Liu, and X. Wu, "Image-based visual servoing of helical microswimmers for planar path following," *IEEE Trans. Autom. Sci. Eng.*, vol. 17, no. 1, pp. 325–333, Jan. 2020.
- [22] O. Bourquardez, R. Mahony, N. Guenard, F. Chaumette, T. Hamel, and L. Eck, "Image-based visual servo control of the translation kinematics of a quadrotor aerial vehicle," *IEEE Trans. Robot.*, vol. 25, no. 3, pp. 743–749, Jun. 2009.
- [23] T. Lee, M. Leok, and N. H. McClamroch, "Geometric tracking control of a quadrotor UAV on SE(3)," in *Proc. 49th IEEE Conf. Decis. Control (CDC)*, Dec. 2010, pp. 5420–5425.
- [24] X. Zhang, J. Jiang, Y. Fang, X. Zhang, and X. Chen, "Enhanced fiducial marker based precise landing for quadrotors," in *Proc. IEEE/ASME Int. Conf. Adv. Intell. Mechatronics (AIM)*, Jul. 2019, pp. 1353–1358.
- [25] T. Hamel and R. Mahony, "Visual servoing of an under-actuated dynamic rigid-body system: An image-based approach," *IEEE Trans. Robot. Autom.*, vol. 18, no. 2, pp. 187–198, Apr. 2002.
- [26] N. Guenard, T. Hamel, and R. Mahony, "A practical visual servo control for an unmanned aerial vehicle," *IEEE Trans. Robot.*, vol. 24, no. 2, pp. 331–340, Apr. 2008.
- [27] R. Mebarki, V. Lippiello, and B. Siciliano, "Nonlinear visual control of unmanned aerial vehicles in GPS-denied environments," *IEEE Trans. Robot.*, vol. 31, no. 4, pp. 1004–1017, Aug. 2015.
- [28] B. Herissé, T. Hamel, R. Mahony, and F.-X. Rusotto, "Landing a VTOL unmanned aerial vehicle on a moving platform using optical flow," *IEEE Trans. Robot.*, vol. 28, no. 1, pp. 77–89, Feb. 2012.
- [29] P. Serra, R. Cunha, T. Hamel, D. Cabecinhas, and C. Silvestre, "Landing of a quadrotor on a moving target using dynamic image-based visual servo control," *IEEE Trans. Robot.*, vol. 32, no. 6, pp. 1524–1535, Dec. 2016.
- [30] H. Zhong *et al.*, "A practical visual servo control for aerial manipulation using a spherical projection model," *IEEE Trans. Ind. Electron.*, vol. 67, no. 12, pp. 10564–10574, Dec. 2020.
- [31] O. Tahri and F. Chaumette, "Point-based and region-based image moments for visual servoing of planar objects," *IEEE Trans. Robot.*, vol. 21, no. 6, pp. 1116–1127, Dec. 2005.
- [32] M. A. Rafique and A. F. Lynch, "Output-feedback image-based visual servoing for multirotor unmanned aerial vehicle line following," *IEEE Trans. Aerosp. Electron. Syst.*, vol. 56, no. 4, pp. 3182–3196, Aug. 2020.
- [33] D. Zheng, H. Wang, J. Wang, S. Chen, W. Chen, and X. Liang, "Image-based visual servoing of a quadrotor using virtual camera approach," *IEEE/ASME Trans. Mechatronics*, vol. 22, no. 2, pp. 972–982, Apr. 2017.
- [34] H. Xie, K. H. Low, and Z. He, "Adaptive visual servoing of unmanned aerial vehicles in GPS-denied environments," *IEEE/ASME Trans. Mechatronics*, vol. 22, no. 6, pp. 2554–2563, Dec. 2017.
- [35] D. Lee, T. Ryan, and H. J. Kim, "Autonomous landing of a VTOL UAV on a moving platform using image-based visual servoing," in *Proc. IEEE Int. Conf. Robot. Autom.*, May 2012, pp. 971–976.
- [36] D. Zheng, H. Wang, W. Chen, and Y. Wang, "Planning and tracking in image space for image-based visual servoing of a quadrotor," *IEEE Trans. Ind. Electron.*, vol. 65, no. 4, pp. 3376–3385, Apr. 2018.
- [37] K. Zhang, Y. Shi, and H. Sheng, "Robust nonlinear model predictive control based visual servoing of quadrotor UAVs," *IEEE/ASME Trans. Mechatronics*, vol. 26, no. 2, pp. 700–708, Apr. 2021.
- [38] D. Zheng, H. Wang, J. Wang, X. Zhang, and W. Chen, "Toward visibility guaranteed visual servoing control of quadrotor UAVs," *IEEE/ASME Trans. Mechatronics*, vol. 24, no. 3, pp. 1087–1095, Jun. 2019.
- [39] H. Xie and A. F. Lynch, "Input saturated visual servoing for unmanned aerial vehicles," *IEEE/ASME Trans. Mechatronics*, vol. 22, no. 2, pp. 952–960, Apr. 2017.



- [40] Z. Cao *et al.*, "Image dynamics-based visual servoing for quadrotors tracking a target with a nonlinear trajectory observer," *IEEE Trans. Syst., Man, Cybern., Syst.*, vol. 50, no. 1, pp. 376–384, Jul. 2020.
- [41] H. Jabbari Asl, "Robust vision-based tracking control of VTOL unmanned aerial vehicles," *Automatica*, vol. 107, pp. 425–432, Sep. 2019.
- [42] A. Abdessameud and F. Janabi-Sharifi, "Image-based tracking control of VTOL unmanned aerial vehicles," *Automatica*, vol. 53, pp. 111–119, Mar. 2015.
- [43] S. Wang, H. Yu, J. Yu, J. Na, and X. Ren, "Neural-network-based adaptive funnel control for servo mechanisms with unknown dead-zone," *IEEE Trans. Cybern.*, vol. 50, no. 4, pp. 1383–1394, Apr. 2020.
- [44] J. Lin, Y. Wang, Z. Miao, H. Zhong, J. Nie, and R. Fierro, "Robust image-based landing control of a quadrotor on an unknown moving platform using circle features," in *Proc. IEEE Int. Conf. Real-time Comput. Robot. (RCAR)*, Jul. 2021, pp. 177–182.
- [45] E. D. Sontag, *Mathematical Control Theory: Deterministic Finite Dimensional Systems*. New York, NY, USA: Springer-Verlag, 1990.
- [46] K. Mohta *et al.*, "Fast, autonomous flight in GPS-denied and cluttered environments," *J. Field Robot.*, vol. 35, no. 1, pp. 101–120, 2018.
- [47] R. Mahony, V. Kumar, and P. Corke, "Multirotor aerial vehicles: Modeling, estimation, and control of quadrotor," *IEEE Robot. Autom. Mag.*, vol. 19, no. 3, pp. 20–32, Sep. 2012.
- [48] J. A. Farrell, M. Polycarpou, M. Sharma, and W. Dong, "Command filtered backstepping," *IEEE Trans. Autom. Control*, vol. 54, no. 6, pp. 1391–1395, Jun. 2009.



**Jie Lin** received the B.S. degree in automation from the College of Electrical Engineering and Automation, Fuzhou University, Fujian, China, in 2019. He is currently pursuing the Ph.D. degree in control science and engineering with Hunan University, Changsha, China.

His current research interests include multi-robot systems, visual servoing, and nonlinear control.



**Yaonan Wang** received the B.S. degree in computer engineering from the East China University of Science and Technology (ECSTU), Fuzhou, China, in 1981, and the M.S. and Ph.D. degrees in electrical engineering from Hunan University, Changsha, China, in 1990 and 1994, respectively.

He has been a Professor with Hunan University since 1995. His current research interests include robotics, intelligent perception and control, and computer vision for industrial applications. He is an academician of the Chinese Academy of Engineering.



**Zhiqiang Miao** (Member, IEEE) received the B.S. and Ph.D. degrees in electrical and information engineering from Hunan University, Changsha, China, in 2010 and 2016, respectively.

From 2014 to 2015, he was a Visiting Scholar with The University of New Mexico, Albuquerque, USA. From 2016 to 2018, he was a Post-Doctoral Fellow with the Department of Mechanical and Automation Engineering, The Chinese University of Hong Kong, Hong Kong, China. Currently, he is an Associate Professor with the College of Electrical and Information Engineering, Hunan University. His research interests include multi-robot systems, visual navigation, and nonlinear control. He was a recipient of the Outstanding Doctoral Dissertation Award of Hunan Province in 2018, the Outstanding Doctoral Dissertation Nomination Award of the Chinese Association of Control in 2018, and the IEEE ROBOTICS AND AUTOMATION LETTERS Best Paper Honorable Mention Award in 2020. He served as the Associate Editor for the ICRA 2022, IROS 2020, and IEEE ARM 2022.



**Hesheng Wang** (Senior Member, IEEE) received the B.Eng. degree in electrical engineering from the Harbin Institute of Technology in 2002 and the M.Phil. and Ph.D. degrees in automation and computer-aided engineering from The Chinese University of Hong Kong, China, in 2004 and 2007, respectively.

He was a Post-Doctoral Fellow and a Research Assistant with the Department of Mechanical and Automation Engineering, The Chinese University of Hong Kong, from 2007 to 2009. He is currently a Professor with the Department of Automation, Shanghai Jiao Tong University. His current research interests include visual servoing, service robot, adaptive robot control, and autonomous driving. He was the General Chair of the IEEE RCAR 2016 and the Program Chair of the IEEE ROBIO 2014 and IEEE/ASME AIM 2019. He served as an Associate Editor for the IEEE TRANSACTIONS ON ROBOTICS from 2015 to 2019. He is an Associate Editor of *Assembly Automation* and the *International Journal of Humanoid Robotics* and a Technical Editor of the IEEE/ASME TRANSACTIONS ON MECHATRONICS.



**Rafael Fierro** (Senior Member, IEEE) received the M.Sc. degree in control engineering from the University of Bradford, U.K., and the Ph.D. degree in electrical engineering from The University of Texas at Arlington.

Before joining UNM, he held a post-doctoral appointment with the General Robotics, Automation, Sensing and Perception (GRASP) Laboratory, University of Pennsylvania; and a faculty position with the Department of Electrical and Computer Engineering, Oklahoma State University. He has been a Professor with the Department of Electrical and Computer Engineering, The University of New Mexico, since 2007. The National Science Foundation (NSF), the U.S. Army Research Laboratory (ARL); the Air Force Research Laboratory (AFRL), Department of Energy (DOE); and Sandia National Laboratories have funded his research. He directs the AFRL-UNM Agile Manufacturing Center and the Multi-Agent, Robotics, and Heterogeneous Systems (MARHES) Laboratory. His current research interests include heterogeneous robotic networks, unmanned aerial systems (UAS), and space robotics for on-orbit servicing. He has served on the Editorial Board of the *Journal of Intelligent and Robotic Systems*, *IEEE Control Systems Magazine*, *IEEE TRANSACTIONS ON CONTROL OF NETWORK SYSTEMS (T-CNS)*, and *IEEE TRANSACTIONS ON AUTOMATION SCIENCE AND ENGINEERING (T-ASE)*. He was the recipient of the Fulbright Scholarship, the National Science Foundation CAREER Award, and the 2008 *International Society of Automation (ISA) Transactions* Best Paper Award.